

www.acsami.org Research Article

Interconnect Fabrication by Electroless Plating on 3D-Printed Electroplated Patterns

Md Emran Hossain Bhuiyan, Salvador Moreno, Chao Wang, and Majid Minary-Jolandan*



Cite This: ACS Appl. Mater. Interfaces 2021, 13, 19271–19281



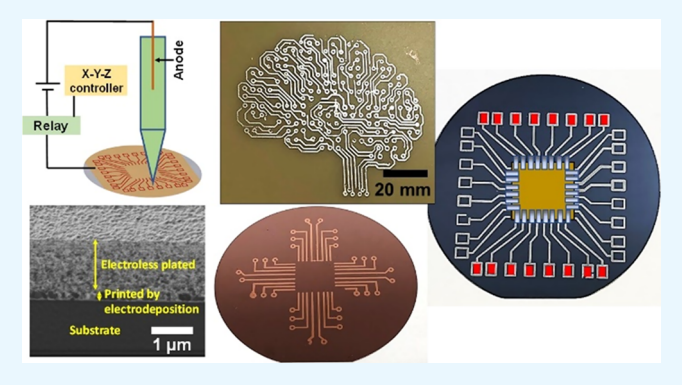
ACCESS

Metrics & More

Article Recommendations

s Supporting Information

ABSTRACT: The metallic interconnects are essential components of energy devices such as fuel cells and electrolysis cells, batteries, as well as electronics and optoelectronic devices. In recent years, 3D printing processes have offered complementary routes to the conventional photolithography- and vacuum-based processes for interconnect fabrication. Among these methods, the confined electrodeposition (CED) process has enabled a great control over the microstructure of the printed metal, direct printing of high electrical conductivity (close to the bulk values) metals on flexible substrates without a need to sintering, printing alloys with controlled composition, printing functional metals for various applications including magnetic applications, and for in situ scanning electron microscope (SEM) nanomechanical experi-



ments. However, the metal deposition rate (or the overall printing speed) of this process is reasonably slow because of the chemical nature of the process. Here, we propose using the CED process to print a single layer of a metallic trace as the seed layer for the subsequent selected-area electroless plating. By controlling the activation sites through printing by the CED process, we control, where the metal grows by electroless plating, and demonstrate the fabrication of complex thin-film patterns. Our results show that this combined process improves the processing time by more than 2 orders of magnitude compared to the layer-by-layer printing process by CED. Additionally, we obtained Cu and Ni films with an electrical resistivity as low as \sim 1.3 and \sim 2 times of the bulk Cu and Ni, respectively, without any thermal annealing. Furthermore, our quantitative experiments show that the obtained films exhibit mechanical properties close to the bulk metals with an excellent adhesion to the substrate. We demonstrate potential applications for radio frequency identification (RFID) tags, for complex printed circuit board patterns, and resistive sensors in a Petri dish for potential biological applications.

KEYWORDS: additive printing of metal films, microscale 3D printing, electroplating, electroless plating, thin films

■ INTRODUCTION

Interconnects are essential components of energy devices such as fuel cells and electrolysis cells, batteries, as well as electronics and optoelectronic devices such as radio frequency identification (RFID) tags, thin-film transistors (TFTs), printed circuit boards (PCB), sensors (thermocouples, temperature, and pressure sensors), and light-emitting devices, among others. Recent significant advances in additive printing (three dimensional (3D) printing) have enabled direct writing of various metals and alloys in desired complex patterns.³⁻ These additive printing processes aim at providing a more flexible, versatile, and often low-cost alternative to the established lithography-based approaches. These processes include direct ink writing (DIW),6-8 electrohydrodynamic printing (EHD),^{9,10} laser-induced forward transfer (LIFT),¹¹⁻¹³ focused electron/ion beam induced deposition (FEBID/FIBID), 14 laser-induced photoreduction (LIPR), 15,16 and confined electrodeposition (CED), 17-19 among others.

Among these processes, CED has been shown to enable a great control over the microstructure of the printed metal from nanocrystalline to nanotwinned, direct printing of high electrical conductivity (close to the bulk values) metals (such as nickel and copper) on flexible substrates without a need to sintering, printing alloys with controlled composition, printing functional metals for various applications including magnetic applications, and for in situ electron microscope nanomechanical experiments. Above the metal deposition rate (or the overall printing speed) of this process is reasonably slow because of the chemical nature of the process, in which pure metals or alloys are synthesized in situ by

Received: January 28, 2021 Accepted: April 3, 2021 Published: April 15, 2021





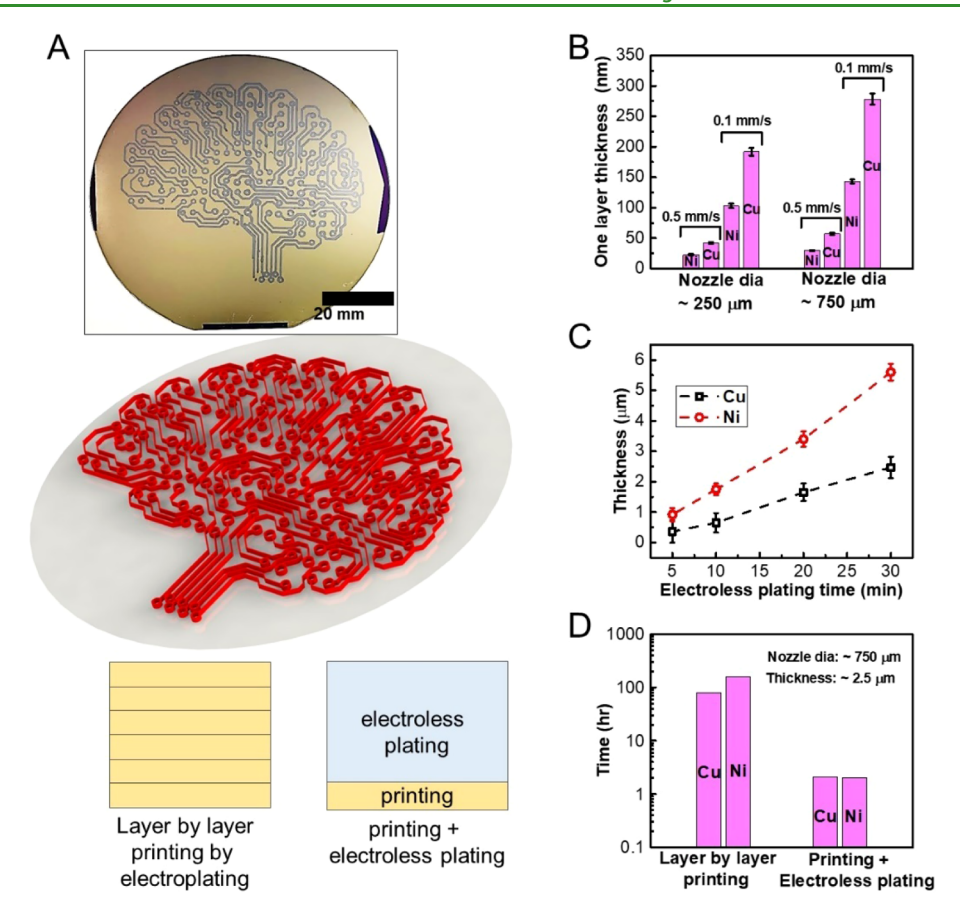


Figure 1. (A) Top and middle panels show the actual print on a wafer and the schematic of the print pattern. The schematic in the bottom compares the concept of layer-by-layer printing by electroplating vs one-layer printing by electroplating followed by electroless plating to obtain the same metal thickness. (B) Thickness dependence of the one-layer metal print by electroplating on the nozzle diameter and nozzle speed. (C) Thickness of the deposited metal vs electroless plating duration. (D) Time comparison of the pattern fabrication by layer-by-layer electroplating vs the combined process (one-layer electroplating followed by electroless plating). Note the log-scale in time.

reduction from an electrolyte. There is a trade-off between the metal quality, purity, and properties on the one hand and the throughput on the other hand.

The thickness of a single-layer metal print in this process can vary from ${\sim}50$ nm upward of ${\sim}300$ nm depending on metal type, the nozzle diameter, and nozzle lateral speed. Nickel has a slower electroplating rate than copper. For example, printing a ${\sim}2~\mu \rm m$ thick Cu trace requires at least five printing cycles, while printing a ${\sim}2~\mu \rm m$ thick Ni trace requires 20 printing cycles. To achieve sufficient film thickness for many practical applications, a large number of layer-by-layer printing cycles should be repeated. Given that the nozzle speed in the CED process is often <1 mm/s, this limitation inherently impedes practical applications of the CED process.

Here, we propose using the CED process to print a single layer of a metallic trace as the seed layer for the subsequent selected-area electroless plating. The general process of the electroless plating involves surface preparation and surface activation by seeding the catalytic metal particles on a substrate. Various methods have been used for printing the seed layer, including reactive inkjet printing and laser writing. After this step, an electroless plating bath is required to deposit metal on the activated surface. By controlling the activation sites through printing by the CED process, we control where the metal grows by electroless plating and demonstrate the fabrication of complex thin-film patterns. Our results show that this combined process

improves the processing time by more than 2 orders of magnitude compared to the layer-by-layer printing process by CED.

■ RESULTS AND DISCUSSION

The pattern fabrication process includes the following steps: printing the desired metal pattern using the CED process on a conductive substrate, removing the unprinted regions of the conductive layer by etching, and finally electroless deposition to obtain the desired film thickness. The details of the CED process can be found in our previous reports^{21,22} and are also summarized in the Materials section. The CAD image and a printed pattern in Figure 1A show an example of complex patterns that can be printed using the CED process at the wafer scale. The bottom panel in Figure 1A schematically shows the cross section of a trace fabricated by layer-by-layer printing vs the hybrid process of electrodeposition printing and electroless plating.

The thickness of the printed metal (or deposition rate) in the CED process depends on the applied current density, the nozzle size, and speed. We estimated the thickness (in microns) of the Cu and Ni films based on the Faraday's law: $t = M \cdot a \cdot i \cdot t \times 100/nF\rho$, in which M is the atomic weight of the metal, a is the current efficiency (CE) ratio, i is the electric current density (A/dm²), t is the time (hours), t is the number of electrons in the electrochemical reaction, t is the Faraday constant, and t0 is the density (g/cm³). 28 Due to potential side

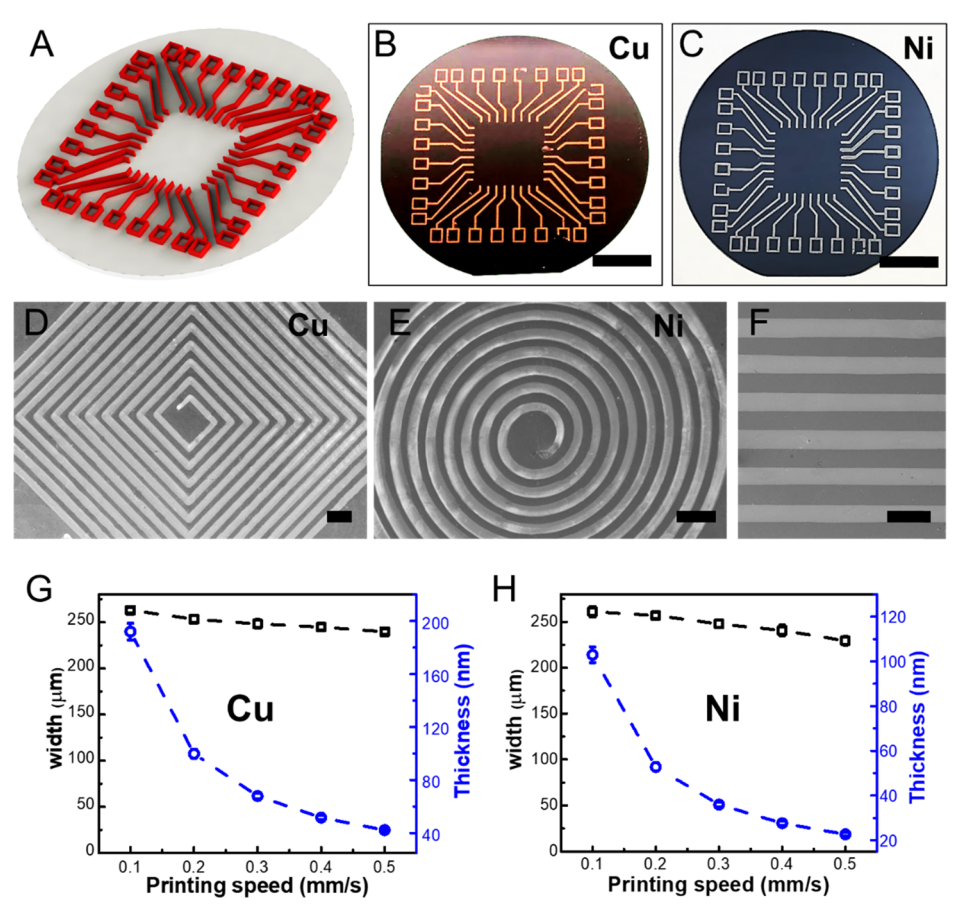


Figure 2. (A) Schematic of the printed patterns in (B) and (C). Optical images of the printed (B) Cu and (C) Ni patterns on a 100 mm silicon wafer, printed by the confined electrodeposition process. The line width in the patterns is \sim 700 μ m. (D–F) SEM micrographs of the printed Cu and Ni patterns with a line width of \sim 250 μ m. The line width and thickness of the printed (G) Cu and (H) Ni lines versus the nozzle speed. The scale bar for the optical images in (B) and (C) is 20 mm, and for the SEM images (D)–(F) is 1 mm.

reactions in the electrodeposition process, the actual thickness may be 5–10% smaller than the theoretical prediction. To calculate the CE, we printed several Cu and Ni traces with two different nozzle sizes at two different nozzle speeds and measured their thicknesses (Figure 1B). To calculate the CE, we compared the measured thickness with the analytically calculated thickness. The CE of printing Cu and Ni in the CED process was calculated to be 95 \pm 3.1 and 96 \pm 2.6%, respectively.

The thickness of the printed metal pattern can be controlled by printing multiple layers²¹ and tailoring the process parameters (e.g., current density, nozzle speed, and electrolyte concentration). However, the multiple passes will increase the device fabrication time. Another approach to increase the thickness is to print metal seeds or precursors on a substrate and then immerse the substrate with activated patterns into an electroless plating bath. In this approach, the printed layer acts as a catalyst for the subsequent electroless plating. In electroless (autocatalytic) plating, chemical reducing agents in the electrolyte reduce metallic ions to solid-state metal. The electroless plating takes place only on the catalytic surfaces. In the Cu and Ni electroless plating, a chemical reducing agent in the electrolyte supplies the electrons to reduce the metal ions:

Cu reduction reaction:
$$Cu^{2+} + 2e \rightarrow Cu$$
 (1)

Ni reduction reaction:
$$Ni^{2+} + 2e \rightarrow Ni$$
 (2)

The deposition rate and final thickness of the electrolessplated layer depend on the plating parameters including deposition time, pH value of the solution, solution composition and complexing agents, electroless plating temperature, and amount and type of additives in the solution. 28 A 10 μ m thick electroless-plated Cu on Cu tracks printed by reaction inkjet printing process in two steps has been reported.²⁹ The thickness of the electroless-plated Ni-P and Cu on a reactive inkjet-printed pattern was measured to be \sim 1.20 μ m, and \sim 1.90 μ m after electroless plating for 5 min at 60 °C. 30 We found that after 30 min of electroless plating, the thicknesses of the Cu and Ni lines were 2.47 and 5.6 μ m, respectively (Figure 1C). We calculated the deposition rate to be $\sim 0.19 \ \mu \text{m/s}$ for Ni and $\sim 0.08 \ \mu \text{m/s}$ for Cu. The deposition time was counted from the instant of immersion of the substrate into the electroless plating solution. It takes ~ 3 to 4 min to reach the mixed (or equilibrium) potential. If the time was counted when the mixed potential was achieved, the deposition rate would slightly increase.²⁸

The direct ink writing or reactive inkjet printing processes have been often used for printing the initial seed layer for electroless plating. ^{27,30,31} In DIW processes, silver inks are used to print the pattern. Silver nanoparticle inks provide excellent electrical conductivity, albeit at a relatively high cost. For largearea printing, non-noble metal nanoparticle inks, such as copper, have been also investigated. ³² However, non-noble metal nanoparticles tend to rapidly oxidize in ambient

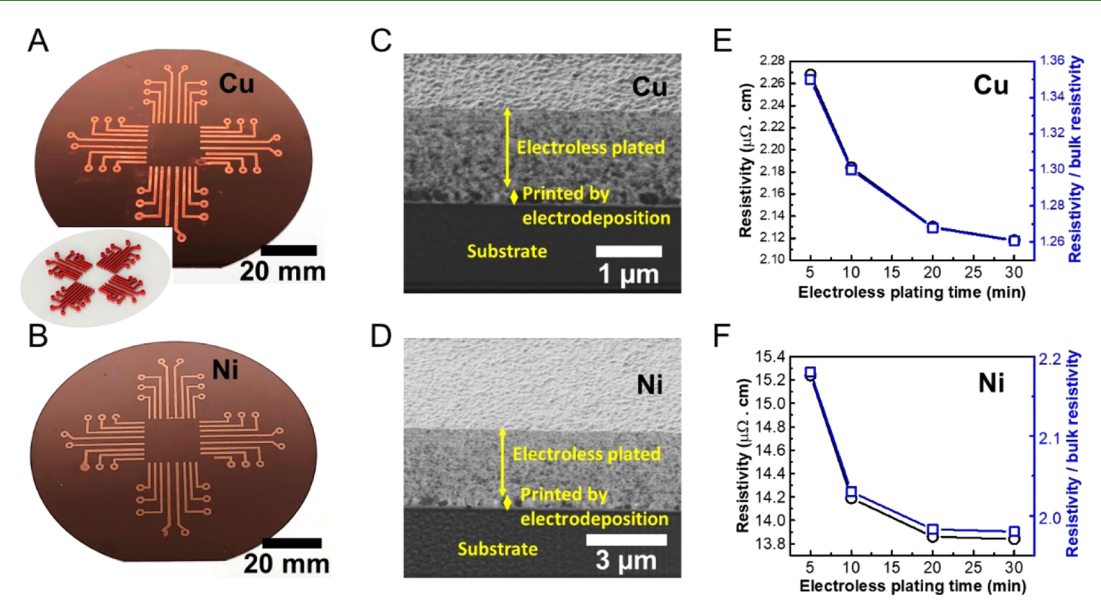


Figure 3. Optical images show the fabricated (A) Cu and (B) Ni interconnects on silicon wafers. The patterns are fabricated by printing one layer by electroplating followed by electroless plating to a final thickness of \sim 2.47 μ m for the Cu pattern and \sim 5.6 μ m for the Ni pattern. The inset shows the schematic of the pattern. The FIB-sectioned cross-sectional images of the (C) Cu and (D) Ni patterns. The films for FIB sectioning are prepared separately by one printed layer and 20 min electroless-plated layer. The electrical resistivity of the (E) Cu and (F) Ni patterns in (A) and (B)

conditions and require a protective carbon³³ or surfactant layer,³⁴ or core—shell structure,³⁵ and post-treatment annealing in an inert atmosphere.³⁶ Laser-induced selective activation processes are also used to fabricate sensors and PCBs on rigid and polymeric substrates.^{37,38} These processes require a coating of filler materials or metals on the substrates to create the pattern. A laser can be also used to directly activate the substrate by making a porous and spongy surface so that palladium chloride in the chemical activation process can infiltrate into the holes for the following electroless plating. The laser beam is scanned 15–20 times on the pattern trajectories to activate the surface. High laser power or a large number of laser passes may degrade polymeric substrates.³⁷

In the electroless plating process, metal also grows on the side walls and may increase the width of the printed interconnects. To investigate the width variation, we measured the width change after 30 min electroless plating. After 30 min of electroless plating for a trace with an initial width of \sim 770 μ m, we measured \sim 0.9 and 1.05% increase in width for Ni and Cu, respectively. From the measurement, we concluded that the percentage of width increment is rather low.

Figure 1D compares the fabrication time of the layer-by-layer electroplating vs the combined process (printing the seed layer by electroplating followed by electroless plating). Our estimation shows that the total time to fabricate a film with a thickness of 2.5 μ m (using a nozzle with a diameter of 750 μ m) reduces by more than 2 orders of magnitude in the combined process compared to the layer-by-layer printing process (Note the log-scale in time).

Figure 2B–F shows optical and scanning electron microscope (SEM) images of various printed Cu and Ni patterns. We considered lines with ~250 and ~750 μ m widths. The patterns were printed at room temperature, have one layer, and were printed with a printing speed of 0.1 mm/s. The printed lines are continuous and fairly uniform in width, which is important for the fabrication of functional devices. By image analysis, we estimated <2% imperfections such as disconti-

nuities or broken lines in the patterns. These imperfections are due to several reasons including meniscus breakage during the printing, weak adhesion of the printed interconnect to the substrate in several regions, and residues of the electrolyte on the printed lines, among others. These imperfections maybe reduced or eliminated through surface engineering to improve the adhesion, reducing the electrolyte spread on the substrate, and using a more stable (vibration and positioning accuracy) printing system to maintain the stable shape of the meniscus during printing.

Given the chemical nature of the CED process, its printing rate is slower than physical printing processes such as inkjet printing and direct ink writing. Although the deposition rate can be increased by optimizing the electrolyte, increasing the cathode temperature, or using an external magnetic field, one of the promising methods to increase the process throughput is using an array of nozzles, as recently demonstrated.³⁹ In this process, multiple nozzles are used to convert the serial printing process to a parallel process.

In the CED process, an electrolyte meniscus between the nozzle tip and the substrate functions as the electrochemical bath. The width (W) of the printed interconnect in CED depends on the meniscus width, which is determined by the nozzle diameter. Since the meniscus moves along with the nozzle, the meniscus width also depends on the nozzle speed (the contact time between the meniscus and the substrate at each point). The dynamic nature of the meniscus width can be defined by the classical Tanner's law, 40 $W \propto V^{3/10} (\gamma t/\eta)^{1/10}$, in which, V is the drop volume, γ is the surface tension, η is the viscosity of the electrolyte, and t is the contact time. From the above equation, for an electrolyte solution, the width of the deposited line mainly depends on the contact time or the nozzle speed, and the wettability or the contact angle, θ , for a constant nozzle height. The nozzle diameter and meniscus height are included as the variables of drop volume. To determine how the printing speed affects the line width, we printed several lines by varying the printing speed ranging from 0.1 to 1 mm/s. For the narrower lines (the nozzle diameter \sim 250 μ m), the speed was increased only up to 0.5 mm/s. The speed was not further increased due to several reasons including unstable meniscus shape, nonuniform line printing, and electrolyte separation from the meniscus. The SEM and optical images shown in Figures S1-S3 confirm that the printed lines are continuous. We found that the line thickness and width decrease with the increase of the nozzle speed (Figures 2G,H and S1-S3,) as predicted by the Faraday's and Tanner's equations. 41 We found that the change in the line thickness vs nozzle speed was much more pronounced compared to the change in line width.

Figure 3A,B shows optical photographs of the Cu and Ni patterns, respectively, after 30 min electroless plating. The patterns were fabricated by printing a single layer using the electroplating process, followed by a selected-area electroless plating process. Optical images showed that metals deposited only on the lines printed by the CED printing. The thicknesses of the Cu and Ni patterns were measured to be ~2.47 and \sim 5.6 μ m, respectively. We prepared separate films for focused ion beam (FIB) sectioning by one printed layer and 20 min electroless-plated layer (Figure 3C,D).

The FIB images show that electroless and printed layers both are fully dense with low or no porosity. The absence of a clear interface between the electroless-plated layer and printed layer indicates that a metallic bond was formed.

The electroplated printed Cu and Ni show excellent electrical properties. It has been shown that five-layer printed Cu and Ni show electrical resistivity 1.7 and 2.4 times of the bulk resistivity, respectively.²¹ However, in the layer-by-layer electroplating printing, the resistivity increases vs the number of layers, possibly due to oxidation of each layer before the next layer is printed, and accumulation of microstructural defects as the number of layers increases.²¹ Here, we measured the electrical resistivity of the films vs the duration of electroless printing (Figure 3E,F). Note that the conductivity of the underlying sputtered thin metal layer was subtracted, and the reported resistivity is for the printed and electrolessplated metal only. We observe that as the electroless plating time increases, the electrical resistivity decreases. The downward trend of the resistivity vs electroless plating duration may be due to incomplete coverage on printed lines and loose microstructural packing. As the plating time progresses, the layer becomes thicker with a dense and continuous microstructure. This growth in Cu and Ni film leads to a more compact grain packing and reduces the electron transfer barrier.42

The 30 min electroless-plated Cu and Ni exhibited a resistivity of \sim 2.12 and \sim 13.84 $\mu\Omega$ ·cm, respectively, 1.26 times of the bulk resistivity (1.68 $\mu\Omega$ ·cm) of Cu and ~1.98 times of the bulk resistivity (6.99 $\mu\Omega$ ·cm) of Ni. Such good electrical conductivity values without any thermal sintering/annealing are an indication of the high quality of the both electroplated printed and electroless-plated metals, as well as their interfaces. We further found that by thermal annealing (200 °C for 1 h in a nitrogen environment), the electrical resistivity is further reduced to about 1.85 and 12.9 $\mu\Omega$ ·cm for Cu and Ni, respectively. The electrical resistivity of the electroless-plated Cu film (300 nm in thickness) has been reported to be \sim 2 to 3 $\mu\Omega$ ·cm, ^{27,43} and it dropped to ~2 $\mu\Omega$ ·cm after annealing for 30 min at 200 °C in a nitrogen environment. 43 The electrical resistivities of the electroless-plated Ni-P and Cu layers on the

reactive inkjet-printed Ni and Cu traces have been reported to be 3.8 \pm 0.2 and 29 \pm 2 $\mu\Omega$, respectively.³⁰

The chemical composition of the films was analyzed by the energy-dispersive X-ray spectroscopy (EDS), Figure 4A,B for

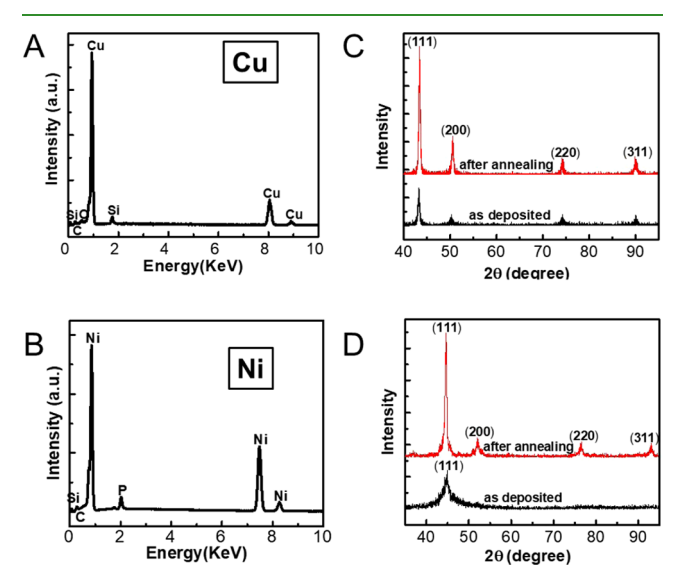


Figure 4. EDS and X-ray diffraction (XRD) spectra, (A) and (C) for Cu and (B) and (D) for Ni, respectively. Each graph shows the XRD spectra of the as-deposited sample and after annealing at 200 °C for 1 h in a nitrogen environment.

Cu and Ni, respectively. The EDS spectra revealed that both metals (Cu and Ni) have no significant amount of impurities. A small peak (corresponding to a weight percentage of ~1.1%) of oxygen was detected in the Cu spectra since Cu tends to rapidly oxidize in air. 4,44 EDS spectra do not show any other impurities such as sulfur (which may be incorporated into the deposited metal from the electrolyte). In the Ni deposition, the weight percentage of Ni in the deposit is ~96.8%, and the phosphorus amount is \sim 3.2%. The Si and C peaks are from the substrate and carbon contamination on the Si wafers.

We characterized the crystal structure by grazing-incidence X-ray diffraction (XRD), Figure 4C,D for Cu and Ni, respectively. The XRD spectra of Cu reveal that Cu is crystalline. In the as-deposited Cu XRD spectra, the peak intensity ratio I(111)/I(200) was 3.52 and the full width at half-maximum (FWHM) of (111) peak was 0.58, which agree with the literature for electroless-plated Cu.²⁹ No other detectable phases such as CuO and Cu2O were detected. The as-deposited Ni showed a broad peak with the FWHM of (111) peak being 3.73. The spectra for the as-deposited Cu contain (111), (200), (220), and (311) peaks, and the spectra for Ni contain (111) peaks, indication of face-centered cubic (fcc) crystal structure. Cu and Ni both have a strong (111) peak. In FCC metals, the {111} plane is the closed pack plane and has the highest electromigration resistance. Therefore, the printed and electroless-plated Cu and Ni can be used in high current density applications.

We also considered the effect of thermal annealing on the crystal structure of the films. After annealing the Cu film at 200 °C for 1 h, the peak intensity ratio increased from 3.52 to 3.65, and the FWHM of (111) decreased from 0.58 to 0.42. All peaks became sharper after ~1 h annealing at 200 °C. After annealing the Ni film, the FWHM of (111) peak decreased from 3.73 to 0.58. In addition, we estimated the grain size

using the Scherrer's equation, $D = K\lambda/\beta \cos \theta$, where D is the crystallite size, K is the shape factor, λ is the X-ray wavelength, β is the FWHM, and θ is the Bragg angle. The grain size of the as-deposited Cu was estimated to be ~19 nm. The grain size of the Cu increased from ~19 to ~26 nm after annealing at 200 °C for 1 h. After annealing, Ni grain size was estimated to be 19.1 nm. The growth in grains with annealing leads to reductions in grain boundary scattering due to charge carriers, thus increases the mobility for the deposited layer, which reduces the resistivity.

To image the surface topography of the electroless-plated Cu and Ni, we used atomic force microscopy (AFM) (Figure 5A,B). The surface roughness from the AFM analysis for the

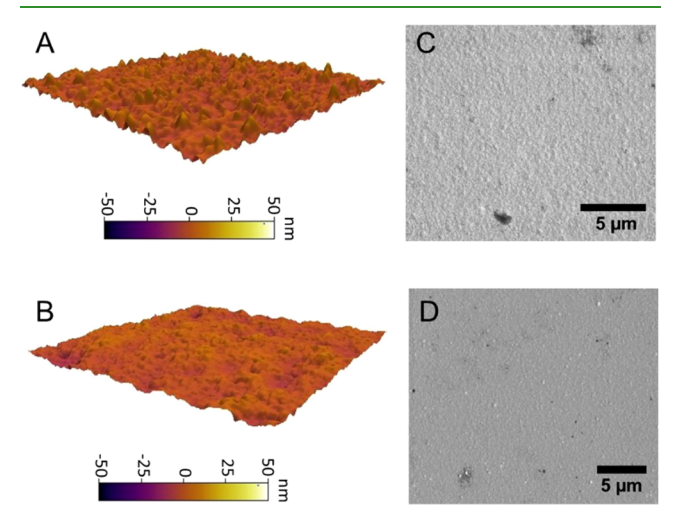


Figure 5. AFM topography and SEM surface morphology images (A), (C) for Cu and (B) and (D) for Ni, respectively.

electroless-plated Cu and Ni layers is 18 ± 5 and 12 ± 4 nm, respectively. The top-view SEM images (Figure 5C,D) also confirm that the Ni surface is smoother than the Cu surface. The electrical and mechanical properties of metals are often affected by the presence of pores and defects. No detectable holes were found in the films, an indication that the deposited layer is fully dense and continuous.

To quantify the mechanical properties of the metal films, we performed a nanoindentation experiment. An array of nanoindentation footprints on the Ni film is shown in Figure 6A. The results of the nanoindentation elastic modulus (E) and hardness (H) are shown in Figure 6B,C. The films (onelayer electroplated printed and 20 min of electroless deposition) show elastic moduli of 124 ± 6.7 and 198 ± 5.4 GPa for Cu and Ni, respectively. As a reference, the elastic modulus for the bulk Cu and Ni are ~133 and ~210 GPa, respectively. In a separate experiment, we printed 20-layer metal films by electroplating to compare with the properties of the hybrid films. The printed Cu exhibited an elastic modulus (E) and hardness (H) of 136 ± 9.68 and 2.64 ± 0.25 GPa, respectively. For printed Ni, the measured E and H were 203 \pm 6.5 and 6.3 \pm 0.34 GPa, respectively. Figure 6D,E shows the comparison of the elastic modulus and hardness obtained in this work with the data from the literature. 45-47 Overall, our data show a good match with the literature. In addition, the properties of the fabricated films are on par with the properties of their bulk counterparts, which is an indication of the good quality of the films.

The reliability of the fabricated patterns depends primarily on how well the films adhere or "stick" to each other and to the substrate. To quantify the adhesion energy of the interface, we used nanoindentation-based techniques by producing welldefined areas of delamination. This method is a mechanicsbased model to calculate the interfacial adhesion energy of an interface using only the site-specific material properties and the dimensions of the delaminated region. No stressed overlayer was introduced to encourage the film delamination. FIB cross sectioning and AFM imaging were used to characterize the delaminated interfaces. The model developed by Cordill et al. 48 was used to calculate the adhesion energy. Details of the experimental and calculation procedure are given in the Supporting Information and Figure S5. A maximum 400 mN

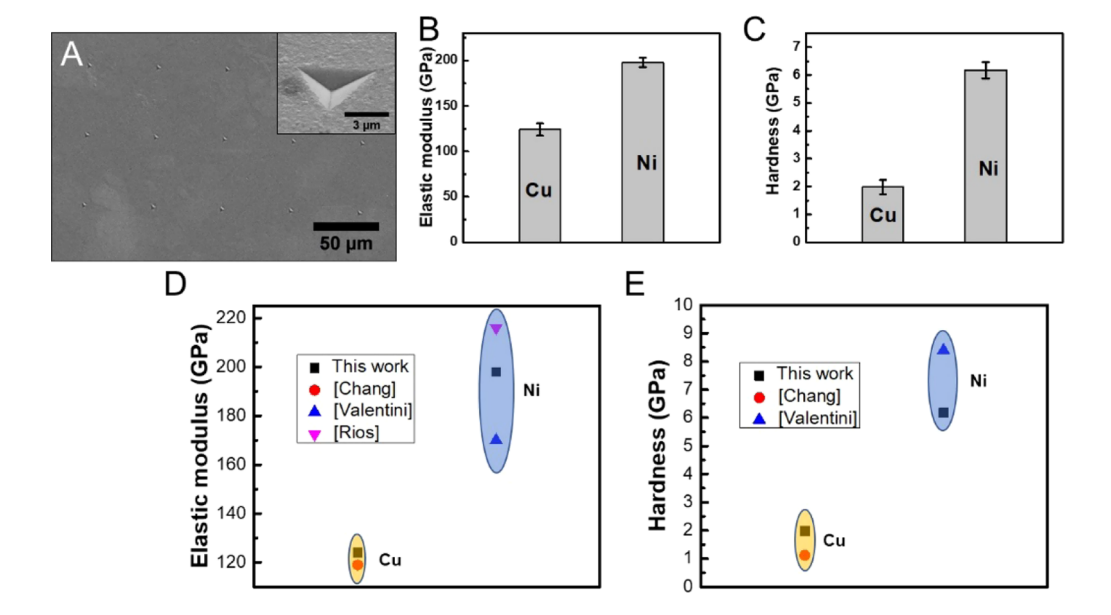


Figure 6. (A) SEM image of an array of nanoindentation footprints on a Ni film. (B) Elastic modulus and (C) hardness of the films obtained from the nanoindentation experiment. The comparison of (D) the elastic modulus and (E) hardness obtained in this work with the data from the literature.45-4

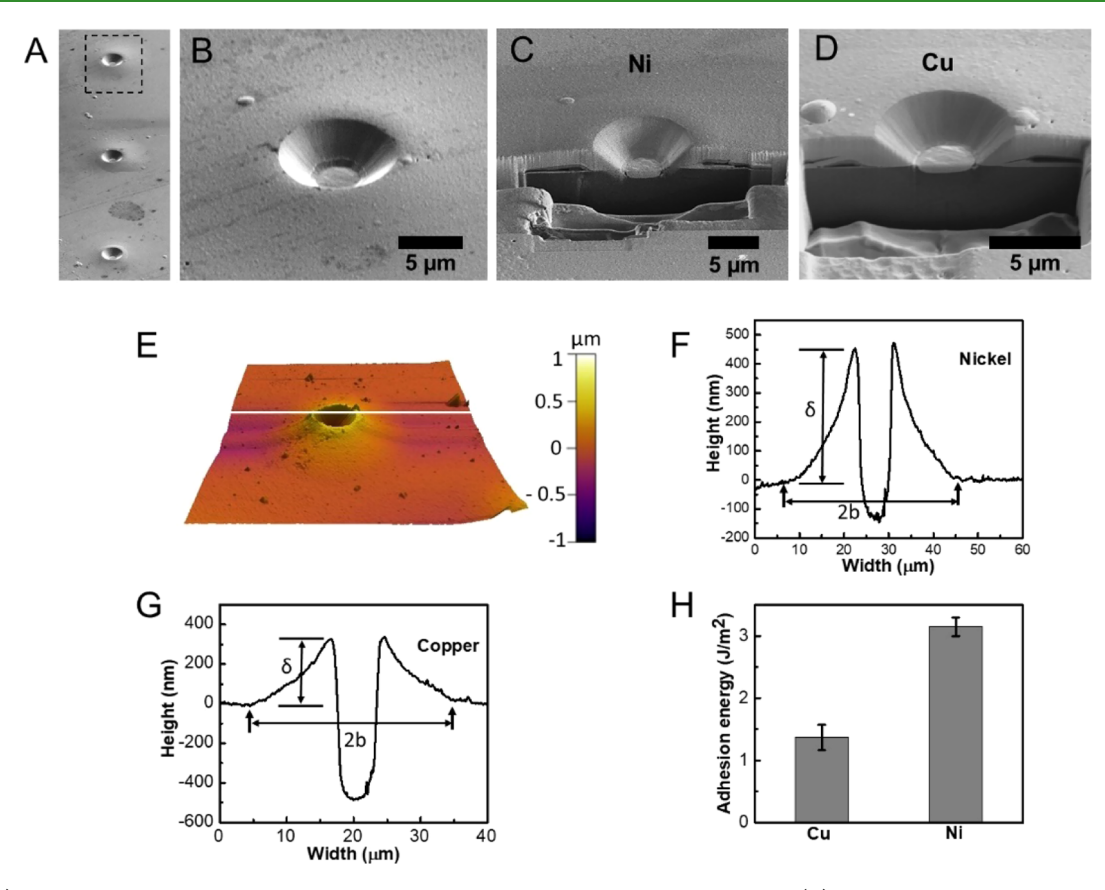


Figure 7. (A) SEM image of an array of buckles produced on a Ni film under a load of 400 mN. (B) Zoomed-in view of one of the indentation footprints encircled in (A). FIB cross-sectional images of indents made on a (C) nickel and a (D) copper film. Both films are fabricated by one electroplated printed layer and 20 min of electroless plating. (E) AFM image of an indentation buckle produces by a load of 400 mN on a nickel film. The white line indicates where the buckling is measured. The AFM topography sections of the indentation buckles produce on (F) nickel and (G) Cu films. (H) Obtained adhesion energy from these experiments.

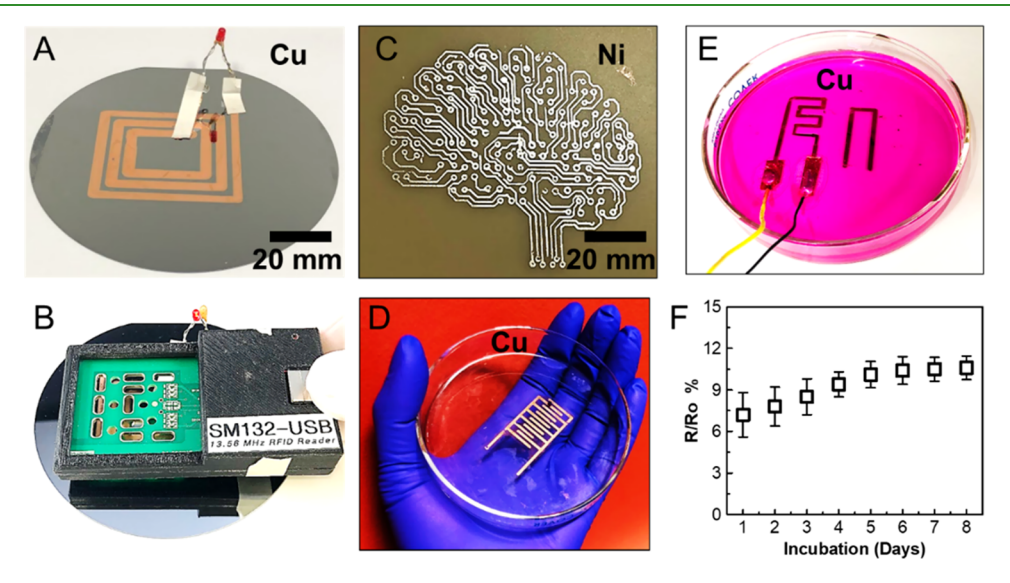


Figure 8. Demonstration of several potential applications of the process. (A) RFID tag made of Cu films on a SI wafer. (B) LED is lit up using wireless power from the RFID reader in (A). (C) Optical image shows a large-area circuit pattern printed on a commercial circuit board. (D) Cu capacitor fabricated inside a glass Petri dish. (E) Cu capacitor inside HBSS buffer after 8 days of incubation. (F) Resistance change of the Cu film over 8 day incubation inside the buffer at 37.5 $^{\circ}$ C (n = 3).

load was applied on the surface, and no radial cracks were observed on the film surface at such a high load. Crosssectional SEM images showed no separation between the electroless-plated and printed layer, which is an indication of a strong bond between these two layers. Delamination happens only between the film and the substrate. The indent and pinned/unpinned buckle geometries were assessed via FIB cross sectioning. Figure 7C,D shows the FIB-polished cross

sections in a tilted view. No radial cracking or spallation of the deposited metal was observed in the applied load range. Indents with loads lower than 50 mN did not produce buckles. We measured the adhesion energy to be 1.57 \pm 0.2 J/m² for Cu and 3.15 \pm 0.15 J/m² for Ni films. The adhesion energy ranging from 0.2 to 2 J/m² has been reported for Cu films prepared by sputter deposition ranging in thickness from 150 to 1500 nm. The adhesion energy for the sputter-deposited 300 nm thick WTi film on Si $_3$ N $_4$ has been reported to be in the range of 1.13–1.36 J/m². 50

As a proof of concept, we demonstrate several possible applications of this process, including a radio frequency identification (RFID) tag, a dense large-area circuit pattern printed on a commercial PCB board, and direct printing of a capacitor-like sensor inside a glass Petri dish for the biological applications. RFID tags have applications in different sectors including medical and military for object tracking and scanning purposes. A RFID tag was demonstrated by printing one Cu layer and 20 min electroless-plated layer (Figure 8A). An LED with a 100 pF capacitor was connected to the RFID tag to show its functionality. A RFID reader, which transmits at 13.56 MHz, was used to wirelessly power the RFID tag. Figure 8B shows the lighted LED when the RFID reader is at a distance of ~15 mm from the RFID tag. When the RFID reader was taken away from the RFID tag, the brightness of the LED decreased. When the RFID reader was at a distance of ~25 mm from the RFID tag, the LED was completely turned off. We also fabricated a Ni circuit pattern on a commercial circuit board substrate. Figure 8D shows a Cu capacitor directly fabricated on a glass Petri dish. Figure 8E shows the capacitor inside HBBS (1x) solution after 8 days. The printed Cu layer showed good adhesion with the Petri dish. Figure 8F shows the change in its resistance over 8 days in 37.5 °C. There was no encapsulation or passivation layer on the Cu lines. Due to the oxidation, the resistance increased in the first few days of the observation period, then it reached a plateau.

CONCLUSIONS

In 3D printing of metal films, there is a trade-off between the film quality (in terms of electrical, mechanical, and material properties) and the printing speed. Chemical processes, such as confided electrodeposition (CED), synthesize high-quality pure and crystalline metals in situ as it is being printed. This process results in lower printing speeds compared to physical methods that deposit the presynthesized metals. The combined electroless plating and electroplating printing proposed in this work aims to resolve the low printing speed issue in the CED process. There remain other challenges that need to be addressed and investigated. Electroless plating of certain metals such as Cu and Ni are well understood, while this knowledge for other metals should be expanded. The properties and microstructure of the electroless-plated films can vary based on process parameters such as the pH, temperature, and electrolyte composition, which require extensive research. If a fine control on the film thickness is required, an accurate analysis should be done to obtain the correlation between the plating duration and film thickness. The effects of postprocessing on the obtained patterns can also be investigated.

■ EXPERIMENTAL SECTION

Materials. The Cu electrolyte consisted of 1 M $CuSO_4$ · SH_2O and 1 M H_2SO_4 in deionized (DI) water. The Ni electrolyte was the

classical Watts's bath⁵¹ consisting of 0.5 M NiSO₄·6H₂O (Sigma-Aldrich), 0.1 M NiCl₂ (Sigma-Aldrich), and 0.7 M H₃BO₃ (Sigma-Aldrich) in DI water. A Cu or Ni wire approximately 0.1 or 0.3 mm in diameter inserted from the backside of the plastic syringe was used as the anode. The printing substrates (cathode) were 500 μ m thick silicon wafers or commercial printed circuit boards. The Cu etchant (APS-100 from Transene Inc) consisting of 15–20% ammonium peroxydisulfate and 80–85% water by weight was used to remove the unprinted Cu blanket layer. The Ni etchant (TFG type from Transene Inc.) consisting of less than 1% thiourea, 10–15% sodium n-nitrobenzene sulfonate, less than 10% sulfuric acid, and more than 75% water by weight was used. For the electroless plating, NI-B (from Transene Inc.) was used for Ni plating, and PC electroless Cu solutions A and B (from Transene Inc.) were used for Cu plating.

Printing Process. Two line widths were considered for the metallic track printing. For larger (700–1000 $\mu m)$ line printing, a plastic syringe was used as the printing head. For the narrower (~100 to 200 μ m) line printing, a glass pipette was used as the printing nozzle. A syringe pump was connected to the plastic syringe to provide electrolyte flow in the nozzle. For the narrower line printing, capillary force and surface tension act as a pump. For noncontinuous patterns, the nozzle should be retracted from the substrate at the end of the print, move to the new spot and again establish the meniscus to continue the printing process, which is time-consuming and may result in less accuracy. To avoid this issue, a relay was connected between the anode and cathode. The GCODE file to send the command to the controller to print the desired patterns was created in the following manner: the circuit pattern was schematically drawn, and for it, a DXF file was created using Solid Works. Conversion of the DXF file to a GCODE was done in ABViewer software. Origin point assignment of the circuit pattern and printing sequence of the segments were done before creating the GCODE in the ABViewer.

Fabrication of Metallic Patterns. To fabricate the conductive substrate, a 30 nm layer of Cu or Ni was deposited using an e-beam vapor deposition system at a pressure lower than 5×10^{-6} Torr and a deposition rate of 0.4 Å/s. Each coating was used for the corresponding metal printing (Cu on Cu and Ni on Ni). For the pattern fabrication, a constant voltage was maintained at -0.4 V for the Cu and -1.2 V for the Ni printing based on our previous work. Wet etching was performed to remove the unprinted initial Cu and Ni layers. After removing the initial conductive metallic layer, the Cuprinted substrate was dipped into the Cu electroless solution. Similarly, the Ni-printed substrate was dipped into the Ni electroless solution. The immersion duration was in the range of 5-30 min depending on the desired thickness. After removal from the plating solution, the samples were rinsed with DI water and then set aside to dry.

Conductivity Measurement. The resistance measurement was done according to the four-point probe method. Initially, the resistivity of the 30 nm Cu and Ni layers deposited using e-beam vapor deposition was measured. Ten millimeters long Cu and Ni lines with one layer were printed on the Cu and Ni substrates, respectively. After printing, the entire substrate was etched to remove the initial deposited Cu and Ni from the unprinted part, followed by electroless plating. To calculate the electrical resistivity, the resistance of the 30 nm deposited Cu/Ni layer under the printed line was subtracted from the total resistance.

To subtract the resistance of the initial e-beam deposited layer, we considered the fabricated line and the e-beam vapor-deposited line as two different resistors connected in parallel, and the parallel resistance

equation
$$\left(\frac{1}{R_{\text{total}}} = \frac{1}{R_{\text{combined process}}} + \frac{1}{R_{\text{e-beam process}}}\right)$$
 was used to obtain

the resistance of the printed and electroless-plated line. To calculate the electrical resistivity, the average cross-sectional area was measured by a stylus profilometer (Veeco Dektek III), and the initial 30 nm ebeam deposited area was subtracted from the average cross-sectional area. The electrical resistivity was calculated using the following equation $\rho = \frac{RA}{I}$.

FIB Sample Preparation. After polishing and cutting the film cross section using a dual-beam FEI NOVA 200 FIB, ion channeling contrast images were obtained from the polished surface. The beam voltage was set at 30 kV and three different currents including high current (5 nA), medium current (1 nA), and low current (0.1 nA) were applied to cut the cross section in several steps. Ion channel images were obtained using a low-energy ion beam (30 KV, 10 pA).

AFM and EDX Sample Preparation and Experiment. The surface roughness analysis was performed using an Asylum Bio3D AFM. To obtain the RMS value of the surface roughness, at least three scans were performed for each sample at different locations. AFM images were recorded over a scan area of 5 μ m \times 5 μ m with a resolution of 512 \times 512 pixels. On the same sample, the elemental analysis was conducted using a ZEISS Supra 40 scanning electron microscope (SEM). The EDS analysis was done at least three times at different points for each sample.

XRD Sample Preparation and Experiment. XRD measurements were performed using a Rigaku Smartlab XRD using a Cu Klpharadiation with a wavelength of λ = 0.15406 nm in the range of 2θ = 35–95°. The scanning step size and speed were $\Delta(2\theta) = 0.01^{\circ}$ and 1°/min, respectively. The voltage and current were set at 40 kV and 44 mA, respectively. The grazing-incidence X-ray diffraction (GIXRD) method was employed to obtain the X-ray diffraction (XRD) spectra. The grazing angle, α , was set at 2° for both samples. In the GIXRD method, the incoming beam and the sample surface angle (α) are kept constant, while the detector is moved along the 2θ circle. The angle between the outgoing beam and sample surface was $2\theta - \alpha$. α should be small enough so that penetration depth (τ = $\sin \alpha/\mu$, where τ is the penetration depth and μ is the attenuation coefficient of the incident beam) of the beam does not exceed the thickness of the targeted film, and at the same time, large enough so that it does not approach the so-called critical angle.⁵

Nanoindentation Experiment. Electroplated printed samples were prepared by printing 20 layers on the SI wafer. The combined samples had one printed layer and 20 min electroless-plated layer. NanoFlip nanoindenter (Nanomechanics, Inc.) equipped with a Berkovich tip was used to perform a nanoindentation test. Each indentation experiment consisted of three steps: loading, holding the indenter at the peak load for 1 s, and unloading. The applied strain rate was 0.05/s and the thermal drift rate was achieved close to 0.2 nm/s before initiating the testing to avoid any error originating due to thermal drift in the measurement. The continuous stiffness measurement (CSM) technique was used to determine the hardness and modulus of elasticity versus the indentation depth.⁵³ Each CSM test returns modulus of elasticity and hardness as a function of indentation depth. To avoid the substrate effects, the indentation depth was set close to 10% of the film thickness and at least 5 times higher than the surface roughness.

ASSOCIATED CONTENT

Supporting Information

The Supporting Information is available free of charge at https://pubs.acs.org/doi/10.1021/acsami.1c01890.

SEM images of the single-layer printed Cu and Ni lines with a nozzle diameter of $\sim 250~\mu m$ for different nozzle speeds; The optical images of single-layer Cu and Ni lines printed with different nozzle speeds, and the width and thickness of the printed Cu and Ni lines vs the nozzle speed; The FIB-sectioned cross-sectional images of Cu and Ni films; and The schematic of an unpinned (top) and pinned (bottom) indentation-induced buckle (PDF)

AUTHOR INFORMATION

Corresponding Author

Majid Minary-Jolandan — Department of Mechanical Engineering, The University of Texas at Dallas, Richardson, Texas 75080, United States; o orcid.org/0000-0003-2472-302X; Email: majid.minary@utdallas.edu

Authors

- Md Emran Hossain Bhuiyan Department of Mechanical Engineering, The University of Texas at Dallas, Richardson, Texas 75080, United States
- Salvador Moreno Department of Mechanical Engineering, The University of Texas at Dallas, Richardson, Texas 75080, United States
- Chao Wang Department of Mechanical Engineering, The University of Texas at Dallas, Richardson, Texas 75080, United States

Complete contact information is available at: https://pubs.acs.org/10.1021/acsami.1c01890

Author Contributions

M.M.J. and M.E.H.B. designed the research. M.E.H.B. performed the experiments and analyzed the data. S.M. helped with the design and manufacturing of the setup and C.W. helped with aspects of the data collection and analysis.

Notes

The authors declare no competing financial interest.

ACKNOWLEDGMENTS

This work was supported by the funding from the US National Science Foundation, CMMI award number 1727539, and the Department of Energy award (DE-SC0017233) subcontract from UHV Technologies, Inc.

REFERENCES

- (1) Hauch, A.; Küngas, R.; Blennow, P.; Hansen, A. B.; Hansen, J. B.; Mathiesen, B. V.; Mogensen, M. B. Recent Advances in Solid Oxide Cell Technology for Electrolysis. *Science* **2020**, 370, No. eaba6118.
- (2) Xu, S.; Zhang, Y.; Cho, J.; Lee, J.; Huang, X.; Jia, L.; Fan, J. A.; Su, Y.; Su, J.; Zhang, H.; Cheng, H.; Lu, B.; Yu, C.; Chuang, C.; Kim, T.-i.; Song, T.; Shigeta, K.; Kang, S.; Dagdeviren, C.; Petrov, I.; Braun, P. V.; Huang, Y.; Paik, U.; Rogers, J. A. Stretchable Batteries with Self-Similar Serpentine Interconnects and Integrated Wireless Recharging Systems. *Nat. Commun.* **2013**, *4*, No. 1543.
- (3) Hirt, L.; Reiser, A.; Spolenak, R.; Zambelli, T. Additive Manufacturing of Metal Structures at the Micrometer Scale. *Adv. Mater.* **2017**, 29, No. 1604211.
- (4) Behroozfar, A.; Daryadel, S.; Morsali, S. R.; Moreno, S.; Baniasadi, M.; Bernal, R. A.; Minary-Jolandan, M. Microscale 3D Printing of Nanotwinned Copper. *Adv. Mater.* **2018**, *30*, No. 1705107.
- (5) Wang, C.; Hossain Bhuiyan, M. E.; Moreno, S.; Minary-Jolandan, M. Direct-Write Printing Copper—Nickel (Cu/Ni) Alloy with Controlled Composition from a Single Electrolyte Using Co-Electrodeposition. ACS Appl. Mater. Interfaces 2020, 12, 18683—18691.
- (6) Ahn, B. Y.; Duoss, E. B.; Motala, M. J.; Guo, X.; Park, S.-I.; Xiong, Y.; Yoon, J.; Nuzzo, R. G.; Rogers, J. A.; Lewis, J. A. Omnidirectional Printing of Flexible, Stretchable, and Spanning Silver Microelectrodes. *Science* **2009**, 323, 1590–1593.
- (7) Skylar-Scott, M. A.; Gunasekaran, S.; Lewis, J. A. Laser-Assisted Direct Ink Writing of Planar and 3D Metal Architectures. *Proc. Natl. Acad. Sci. U.S.A.* **2016**, *113*, 6137–6142.
- (8) Ladd, C.; So, J. H.; Muth, J.; Dickey, M. D. 3D printing of Free Standing Liquid Metal Microstructures. *Adv. Mater.* **2013**, 25, 5081–5085.
- (9) Park, J.-U.; Hardy, M.; Kang, S. J.; Barton, K.; Adair, K.; kishore Mukhopadhyay, D.; Lee, C. Y.; Strano, M. S.; Alleyne, A. G.; Georgiadis, J. G.; Ferreira, P. M.; Rogers, J. A. High-Resolution Electrohydrodynamic Jet Printing. *Nat. Mater.* **2007**, *6*, 782–789.

- (10) Lee, D.; Hwang, E.; Yu, T.; Kim, Y.; Hwang, J. Structuring of Micro Line Conductor Using Electro-Hydrodynamic Printing of a Silver Nanoparticle Suspension. *Appl. Phys. A* **2006**, 82, 671–674.
- (11) Bohandy, J.; Kim, B.; Adrian, F. Metal Deposition from a Supported Metal Film using an Excimer Laser. *J. Appl. Phys.* **1986**, *60*, 1538–1539.
- (12) Zenou, M.; Sa'Ar, A.; Kotler, Z. Laser Jetting of Femto-Liter Metal Droplets for High Resolution 3D Printed Structures. *Sci. Rep.* **2015**, *5*, No. 17265.
- (13) Wang, J.; Auyeung, R. C. Y.; Kim, H.; Charipar, N. A.; Piqué, A. Three-Dimensional Printing of Interconnects by Laser Direct-Write of Silver Nanopastes. *Adv. Mater.* **2010**, *22*, 4462–4466.
- (14) Botman, A.; Mulders, J.; Hagen, C. Creating Pure Nanostructures from Electron-Beam-Induced Deposition using Purification Techniques: A Technology Perspective. *Nanotechnology* **2009**, *20*, No. 372001.
- (15) Tanaka, T.; Ishikawa, A.; Kawata, S. Two-Photon-Induced Reduction of Metal Ions for Fabricating Three-Dimensional Electrically Conductive Metallic Microstructure. *Appl. Phys. Lett.* **2006**, *88*, No. 081107.
- (16) Fan, G.; Han, Y.; Luo, S.; Li, Y.; Qu, S.; Wang, Q.; Gao, R.; Chen, M.; Han, M. Mechanism for the Photoreduction of Poly (vinylpyrrolidone) to HAuCl 4 and the Dominating Saturable Absorption of Au Colloids. *Phys. Chem. Chem. Phys.* **2016**, *18*, 8993–9004.
- (17) Hu, J.; Yu, M.-F. Meniscus-Confined Three-Dimensional Electrodeposition for Direct Writing of Wire Bonds. *Science* **2010**, 329, 313–316.
- (18) Daryadel, S.; Behroozfar, A.; Morsali, S. R.; Moreno, S.; Baniasadi, M.; Bykova, J.; Bernal, R. A.; Minary-Jolandan, M. Localized Pulsed Electrodeposition Process for Three-Dimensional Printing of Nanotwinned Metallic Nanostructures. *Nano Lett.* **2018**, 18, 208–214.
- (19) Hirt, L.; Ihle, S.; Pan, Z.; Dorwling-Carter, L.; Reiser, A.; Wheeler, J. M.; Spolenak, R.; Vörös, J.; Zambelli, T. Template-Free 3D Microprinting of Metals Using a Force-Controlled Nanopipette for Layer-by-Layer Electrodeposition. *Adv. Mater.* **2016**, *28*, 2311–2315.
- (20) Daryadel, S.; Behroozfar, A.; Minary-Jolandan, M. Toward Control of Microstructure in Microscale Additive Manufacturing of Copper Using Localized Electrodeposition. *Adv. Eng. Mater.* **2019**, *21*, No. 1800946.
- (21) Bhuiyan, M. E. H.; Behroozfar, A.; Daryadel, S.; Moreno, S.; Morsali, S.; Minary-Jolandan, M. A Hybrid Process for Printing Pure and High Conductivity Nanocrystalline Copper and Nickel on Flexible Polymeric Substrates. *Sci. Rep.* **2019**, *9*, No. 19032.
- (22) Behroozfar, A.; Bhuiyan, M. E. H.; Daryadel, S.; Edwards, D.; Rodriguez, B. J.; Minary-Jolandan, M. Additive Printing of Pure Nanocrystalline Nickel Thin Films Using Room Environment Electroplating. *Nanotechnology* **2019**, *31*, No. 055301.
- (23) Daryadel, S.; Behroozfar, A.; Minary-Jolandan, M. A Microscale Additive Manufacturing Approach for in situ Nanomechanics. *Mater. Sci. Eng. A* **2019**, 767, No. 138441.
- (24) Daryadel, S.; Minary-Jolandan, M. Thermal Stability of Microscale Additively Manufactured Copper Using Pulsed Electrodeposition. *Mater. Lett.* **2020**, 280, No. 128584.
- (25) Xu, Z.; Huang, J.; Zhang, C.; Daryadel, S.; Behroozfar, A.; McWilliams, B.; Boesl, B.; Agarwal, A.; Minary-Jolandan, M. Bioinspired Nacre-Like Ceramic with Nickel Inclusions Fabricated by Electroless Plating and Spark Plasma Sintering. *Adv. Eng. Mater.* **2018**, 20, No. 1700782.
- (26) Ratautas, K.; Andrulevičius, M.; Jagminienė, A.; Stankevičienė, I.; Norkus, E.; Račiukaitis, G. Laser-Assisted Selective Copper Deposition on Commercial PA6 by Catalytic Electroless Plating Process and Activation Mechanism. *Appl. Surf. Sci.* **2019**, 470, 405—410.
- (27) Liao, Y.-C.; Kao, Z.-K. Direct writing patterns for electroless plated copper thin film on plastic substrates. *ACS Appl. Mater. Interfaces* **2012**, *4*, 5109–5113.

- (28) Schlesinger, M.; Paunovic, M. Modern Electroplating; John Wiley & Sons, 2011; Vol. 55.
- (29) Chen, J.-J.; Lin, G.-Q.; Wang, Y.; Sowade, E.; Baumann, R. R.; Feng, Z.-S. Fabrication of Conductive Copper Patterns using Reactive Inkjet Printing Followed by Two-Step Electroless Plating. *Appl. Surf. Sci.* **2017**, *396*, 202–207.
- (30) Petukhov, D. I.; Kirikova, M. N.; Bessonov, A. A.; Bailey, M. J. Nickel and Copper Conductive Patterns Fabricated by Reactive Inkjet Printing Combined with Electroless Plating. *Mater. Lett.* **2014**, *132*, 302–306.
- (31) Cheng, K.; Yang, M. H.; Chiu, W. W.; Huang, C. Y.; Chang, J.; Ying, T. F.; Yang, Y. Ink-Jet Printing, Self-Assembled 0Polyelectrolytes, and Electroless Plating: Low Cost Fabrication of Circuits on a Flexible Substrate at Room Temperature. *Macromol. Rapid Commun.* 2005, 26, 247–264.
- (32) Lee, Y.; Choi, J.-r.; Lee, K. J.; Stott, N. E.; Kim, D. Large-Scale Synthesis of Copper Nanoparticles by Chemically Controlled Reduction for Applications of Inkjet-Printed Electronics. *Nanotechnology* **2008**, *19*, No. 415604.
- (33) Li, J.; Liu, C.-Y. Carbon-Coated Copper Nanoparticles: Synthesis, Characterization and Optical Properties. *New J. Chem.* **2009**, 33, 1474–1477.
- (34) Ang, T.; Wee, T.; Chin, W. Three-dimensional Self-assembled Monolayer (3D SAM) of n-alkanethiols on Copper Clusters. *J. Phys. Chem. B* **2004**, *108*, 11001–11010.
- (35) Tsuji, M.; Hikino, S.; Sano, Y.; Horigome, M. Preparation of Cu@ Ag Core—Shell Nanoparticles Using a Two-Step Polyol Process Under Bubbling of N2 Gas. *Chem. Lett.* **2009**, *38*, 518—519.
- (36) Jang, S.; Seo, Y.; Choi, J.; Kim, T.; Cho, J.; Kim, S.; Kim, D. Sintering of Inkjet Printed Copper Nanoparticles for Flexible Electronics. *Scr. Mater.* **2010**, *62*, 258–261.
- (37) Zhang, Y.; Tang, P. T.; Hansen, H. N.; Nielsen, J. S. Electroless Plating on Plastic Induced by Selective Laser Activation. *Plat. Surf. Finish.* **2010**, *97*, 43–47.
- (38) Ratautas, K.; Andrulevičius, M.; Jagminienė, A.; Stankevičienė, I.; Norkus, E.; Račiukaitis, G. Laser-assisted selective copper deposition on commercial PA6 by catalytic electroless plating—Process and activation mechanism. *Appl. Surf. Sci.* **2019**, 470, 405—410
- (39) Lin, Y. P.; Zhang, Y.; Yu, M. F. Parallel Process 3D Metal Microprinting. Adv. Mater. Technol. 2019, 4, No. 1800393.
- (40) Tanner, L. The Spreading of Silicone Oil Drops on Horizontal Surfaces. *J. Phys. D: Appl. Phys.* **1979**, *12*, 1473–1484.
- (41) Lei, Y.; Zhang, X.; Xu, D.; Yu, M.; Yi, Z.; Li, Z.; Sun, A.; Xu, G.; Cui, P.; Guo, J. Dynamic "Scanning-Mode" Meniscus Confined Electrodepositing and Micropatterning of Individually Addressable Ultraconductive Copper Line Arrays. *J. Phys. Chem. Lett.* **2018**, *9*, 2380–2387
- (42) Zabetakis, D.; Loschialpo, P.; Smith, D.; Dinderman, M. A.; Dressick, W. J. Direct-Write Patterning Palladium Colloids as a Catalyst for Electroless Metallization for Microwave Composites. *Langmuir* **2009**, 25, 1785–1789.
- (43) Shacham-Diamand, Y. Y. Electroless Copper Deposition using Glyoxylic Acid as Reducing Agent for Ultralarge Scale Integration Metallization. *Electrochem. Solid-State Lett.* **2000**, *3*, 279–282.
- (44) Daryadel, S.; Behroozfar, A.; Morsali, S. R.; Moreno, S.; Baniasadi, M.; Bykova, J.; Bernal, R. A.; Minary-Jolandan, M. Localized Pulsed Electrodeposition Process for Three-Dimensional Printing of Nanotwinned Metallic Nanostructures. *Nano Lett.* **2018**, 18, 208–214.
- (45) Domínguez-Ríos, C.; Hurtado-Macias, A.; Torres-Sánchez, R.; Ramos, M. A.; González-Hernández, J. Measurement of Mechanical Properties of an Electroless Ni-B Coating Using Nanoindentation. *Ind. Eng. Chem. Res.* **2012**, *51*, 7762–7768.
- (46) Valentini, R.; Cavaliere, P.; Valerini, D. Nanoindentation and Scratch Behaviour of Ni–P Electroless Coatings. *Tribol.-Mater., Surf. Interfaces* **2020**, *14*, 22–32.

- (47) Chang, S.-Y.; Chang, T.-K. Grain Size Effect on Nanomechanical Properties and Deformation Behavior of Copper under Nanoindentation Test. *J. Appl. Phys.* **2007**, *101*, No. 033507.
- (48) Cordill, M. J.; Bahr, D. F.; Moody, N. R.; Gerberich, W. W. Recent Developments in Thin Film Adhesion Measurement. *IEEE Trans. Device Mater. Reliab.* **2004**, *4*, 163–168.
- (49) Kriese, M. D.; Gerberich, W. W.; Moody, N. R. Quantitative Adhesion Measures of Multilayer Films: Part II. Indentation of W/Cu, W/W, Cr/W. J. Mater. Res. 1999, 14, 3019–3026.
- (50) Kleinbichler, A.; Pfeifenberger, M.; Zechner, J.; Moody, N.; Bahr, D.; Cordill, M. New Insights into Nanoindentation-Based Adhesion Testing. *JOM* **2017**, *69*, 2237–2245.
- (51) DiBari, G. A. Nickel Plating. Met. Finish. 1999, 97, 289-290.
- (52) Birkholz, M. Thin Film Analysis by X-Ray Scattering; John Wiley & Sons, 2006.
- (53) Hay, J.; Agee, P.; Herbert, E. Continuous Stiffness Measurement During Instrumented Indentation Testing. *Exp. Tech.* **2010**, *34*, 86–94.

Supporting Information

Interconnect Fabrication by Electroless Plating on 3D-Printed Electroplated Patterns

Md Emran Hossain Bhuiyan, Salvador Moreno, Chao Wang, and Majid Minary-Jolandan*

Department of Mechanical Engineering, The university of Texas at Dallas, Richardson, TX 75080, United Stated of America

*E-mail: majid.minary@utdallas.edu

Current efficiency calculation

To calculate the current efficiency (CE) of the Cu and Ni electroplating at various printing speeds, the theoretical thickness of the one-layer Cu and Ni printed line was obtained using $t = \frac{M.a.i.t \times 100}{nF\rho}$, in which M is the atomic mass of the metal, a is the current efficiency ratio (used a = 1 when theoretical calculation was done), i is the electric current density (in A/dm²), t is the time (in hours), t is the number of electrons in the electrochemical reaction (t = 2 for both Cu and Ni electroplating), t is the Faraday constant (26.799 A-h/mol), and t is the density (in g.cm-³). The molar mass (t) of Cu and Ni was used as 63.546 g/mol, and 58.693 gm/mol, respectively. The density (t) of copper and nickel is 8.96 g/cm³, and 8.907 g/cm³, respectively. Several profilometer scans were taken to obtain the average thickness of the single layer printed Cu and Ni. The measured thickness was divided by the theoretical value to obtain the current efficiency.

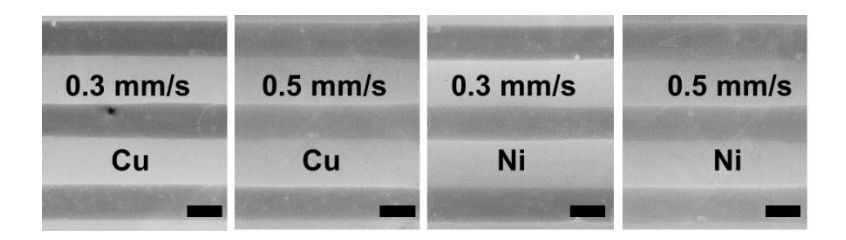


Figure S1. The SEM images of the single-layer printed Cu and Ni lines with a nozzle diameter of ~250 μ m for different nozzle speeds. The scale bar for all SEM images is 250 μ m.

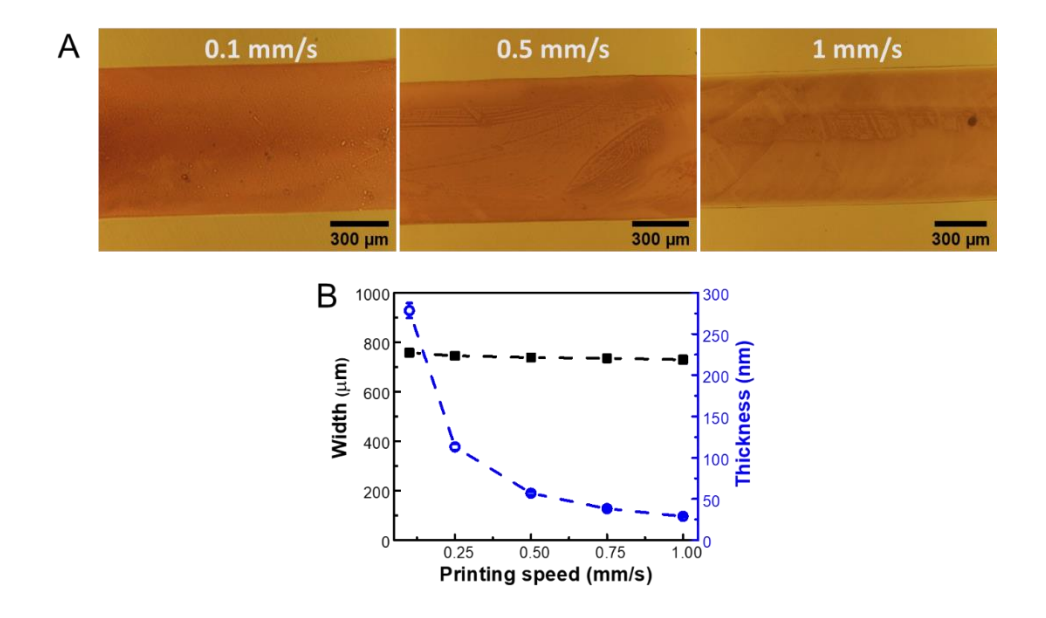


Figure S2. (A) The optical images of single layer Cu lines printed with different nozzle speeds. (B) The width and thickness of the printed Cu lines vs. the nozzle speed. The lines were printed with a nozzle diameter of \sim 750 μ m.

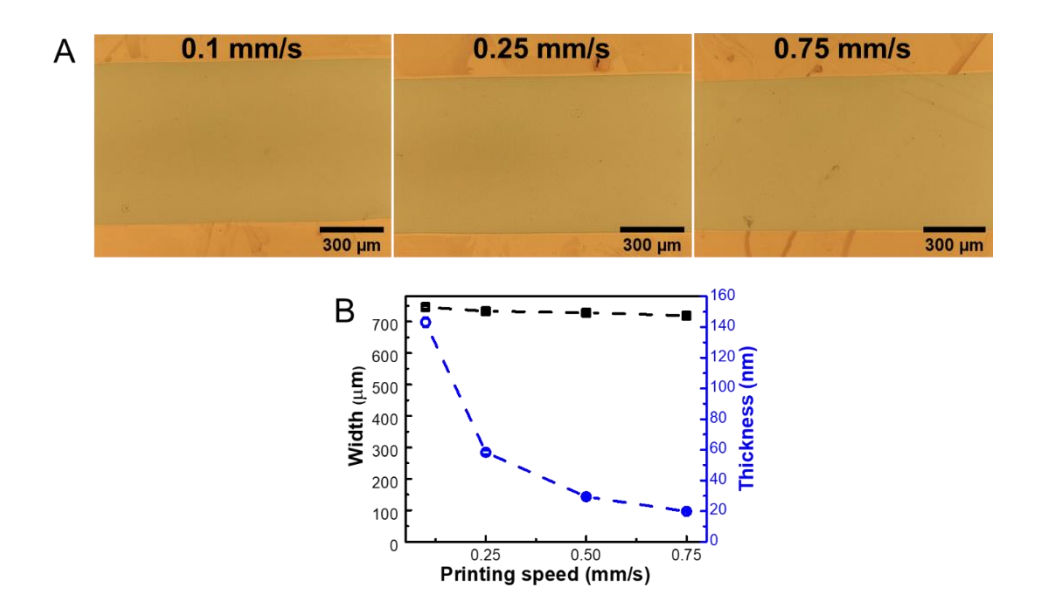


Figure S3. (A) The optical images of single layer Ni lines printed with different nozzle speeds. (B) The width and thickness of the printed Ni lines vs. the nozzle speed. The lines were printed with a nozzle diameter of \sim 750 μ m.

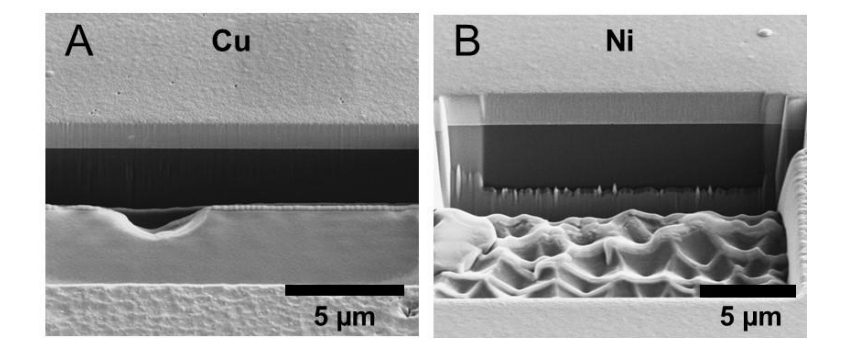


Figure S4. The FIB sectioned cross-section images of the (A) Cu and (B) Ni films.

Adhesion energy measurement

The films investigated consisted of one printed layer and 20 minutes electroless plated layer on a silicon wafer (~ 500 µm thick). The indentation experiment was conducted with an Agilant G200 nanoindenter. A 90° conical diamond tip with a 3 µm tip-diameter and a load range between 250 mN and 400 mN was used to generate indentation-induced delamination. Three indents were made per maximum load in this range, which was increased in intervals of 50 mN. The indents were set in a grid being 50 µm apart from each other to avoid any interaction of the formed blisters. After indentation, each resulting delamination was imaged with an AFM. The buckle/blister heights and widths were used in the subsequent adhesion mechanics to calculate the interfacial adhesion energy values. The elastic moduli of the printed and electroless plated metals was determined from the nanoindentation experiments using the continuous stiffness method.

When nanoindentation is used to initiate delamination, the size of the resulting blister, the load-depth curve, and the shape of the blister cross-section are important parameters to confirm whether the blister is pinned or unpinned. Pinned and unpinned conditions are schematically shown in Figure. S5. Examination of the blister cross-section is a way to determine the pinned/unpinned nature of the blister. Indentation blisters are modeled as circular blisters using the Hutchinson and Suo model ¹, because the indentation initiated the delamination. By measuring the dimensions of the blister, the effective driving stress (the stress which caused a specific blister) can be determined.

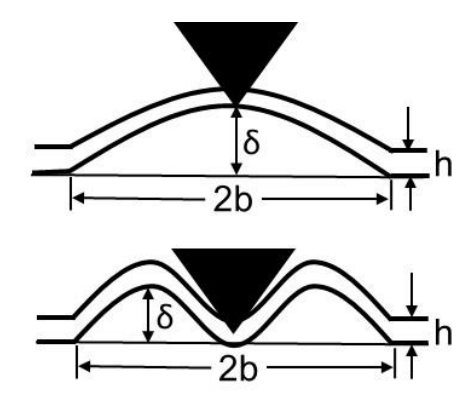


Figure S5. The schematic of an unpinned (top) and pinned (bottom) indentation-induced buckle.

The critical buckling stress, σ_b , and the driving stress, σ_d , of the film depend on the film thickness, h, the radius of the buckle, b, and the height of the buckle, δ (Fig. S5). Using the Hutchinson and Suo's model ¹, the critical buckling stress and driving stress are given by:

$$\sigma_b = \frac{\mu^2 E}{12 (1 - v^2)} \left(\frac{h}{b}\right)^2 \tag{1}$$

$$\sigma_d = \sigma_b \left(c_1 \left(\frac{\delta}{h} \right)^2 + 1 \right) \tag{2}$$

Where μ^2 is 14.68 for an unpinned blister, and 42.67 if the blister is pinned at the center (Figure. S5) and $C_1=0.2473~(1+v)+0.2231~(1-v^2)^2$. The adhesion energy, $\Gamma(\Psi)$ is calculated using:

$$\Gamma(\Psi) = C_2 \left(1 - \left(\frac{\sigma_b}{\sigma_d} \right)^2 \right) \frac{(1 - v)h\sigma_d}{E}$$
 (3)

where $C_2 = (1 + 0.9021 (1 - v))^{-1}$ The term Ψ is the phase angle of loading.

$$\Psi = tan^{-1}(4\cos\omega + \sqrt{3} \gamma \sin \omega / -4\sin\omega + \sqrt{3} \gamma \cos\omega)$$
 (4)

where ω is 52.1° ² and $\gamma = \delta/h$. When the phase angle of loading is 0°, then the adhesion energy is determined entirely from the normal forces. When the crack is under pure shear, the phase angle of loading is ± 90°. The calculated phase angle was obtained to be - 42.93° and - 41.39°, for Cu and Ni, respectively.

Glass nozzles with tip diameters of ~10 μm to 250 μm were fabricated (Figure S6). For a diameter of up to ~ 30 μm , the nozzle can be directly fabricated using a pipette puller. However, for larger diameters, the pulled nozzle is cut at the desired diameter using a sharp ceramic knife. Figure S7 shows the SEM images of the printed metallic traces with linewidths in the range of ~ 10 μm to ~ 110 μm .

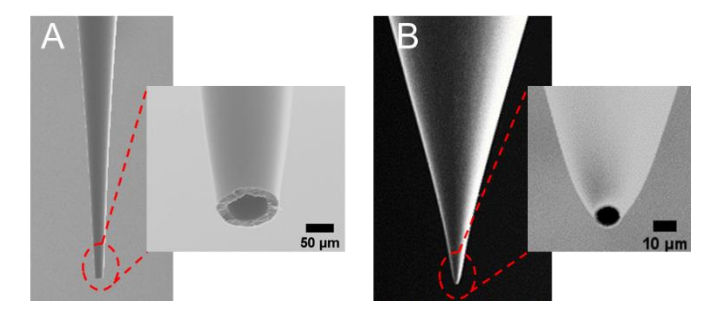


Figure S6 The scanning electron microscopy (SEM) images of the (A) \sim 100 μ m, and (B) \sim 10 μ m glass nozzle fabricated by a pipette puller.

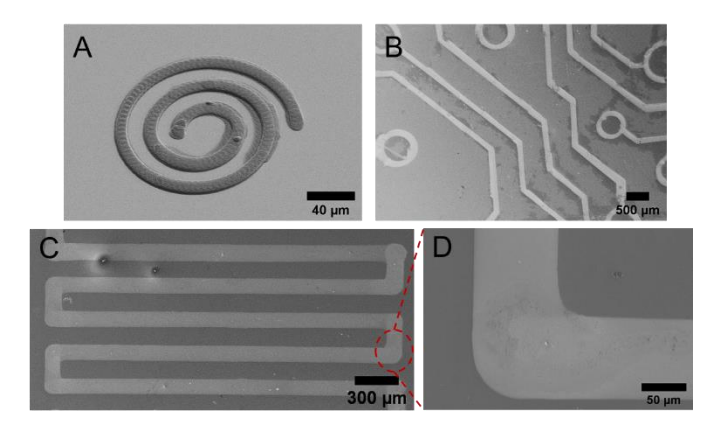


Figure S7 The SEM images of printed metallic traces with a line width of (A) \sim 10 μ m, (B) \sim 110 μ m, and (C) \sim 90 μ m. (D) A zoomed-in-view of a corner shown in C.

The adhesion of the printed and electroless plated Cu and Ni lines were qualitatively assessed by the tape peel test (Figure S8). A tape (Scotch 600, 3M) was adhered to the sample lines and removed by peeling. The sample lines demonstrated good adhesion on the Si wafer. Subsequent to adhesive tape attachment and removal, no evidence of delamination or structural change was observed and the printed and electroless plated metal traces remained intact.

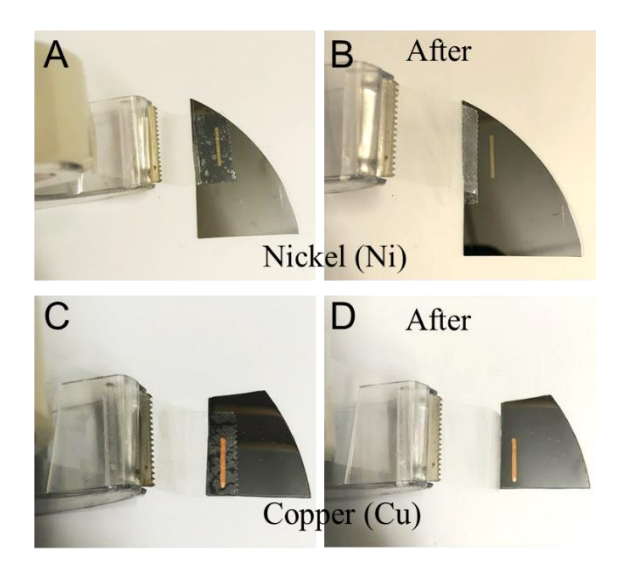


Figure S8 The tape peeling test conducted on (A) and (B) Ni, and (C) and (D) Cu patterns fabricated by a single layer of electroplating printing and 20 minutes of electroless plating.

References

- 1. Hutchinson, J. W.; Suo, Z., Mixed mode cracking in layered materials. In *Advances in applied mechanics*, Elsevier: 1991; Vol. 29, pp 63-191.
- 2. Callister, W. D., *Fundamentals of materials science and engineering*. Wiley London: 2000; Vol. 471660817.